Supporting Information

In-situ Craft of a 3D N-doped Carbon/Defective $V_2O_{5-x}\cdot nH_2O$ Nanosheets Composite for High Performance Fibrous Flexible Zn-ion Batteries

Rui Pan[a], Anqi Zheng[a], Bing He[c], Yuwei Xiong[a], Fengsai Han[b], Lei Wei[c], Qingwen Li*[,b], Qichong Zhang*[,b], Kuibo Yin*[,a],Litao Sun*[,a]

a. SEU-FEI Nano-Pico Center, Key Laboratory of MEMS of Ministry of Education, Southeast University, Nanjing, 210096, China

b. Key Laboratory of Multifunctional Nanomaterials and Smart Systems, Suzhou Institute of Nano-Tech and Nano-Bionics, Chinese Academy of Sciences, Suzhou 215123, China

c. School of Electrical and Electronic Engineering, Nanyang Technological University, 50 Nanyang Avenue, 639798, Singapore

[*]E-mail: qwli2007@sinano.ac.cn

qczhang2016@sinano.ac.cn

yinkuibo@seu.edu.cn

slt@seu.edu.cn.

Fabrication of NC@CNTF

Similar to the previous work, NC@CNTF was prepared via an etching-after-solution process. First, CNTFs were cleaned with ethanol and deionized water. Cobalt nitrate hexahydrate (0.582 g) was dissolved in 40 mL of water to form solution A, and 1.34 g of 2-methylimidazole was dissolved in 40 mL of water to form solution B. After keeping magnetic stirring for 15 min, two solution is to form a purple solution and the pretreated CNTFs were placed into it for reacting for 4 h at room temperature, the CNTFs were taken out and rinsed with deionized water. Then, the obtained Co-based MOF was thermally treated in a tube furnace at 800 °C for 2 h with a heating rate of 1 °C min^{-1} in an atmosphere of 5% H_2/Ar. Finally, a solution (3 M $FeCl_3$ and 0.36 mM HCl) was used to remove Co from the carbon skeletons by immersing the obtained CNTFs overnight. After being washed and dried at 60 °C for 12 h, the high-conductivity 3D porous N-doped carbon nanowall arrays on the CNTFs were obtained (NC@CNTF).

Fabrication of VO@NC@CNTF

First, a mixture of 0.3 mL vanadium oxytriisopropoxide and 45 ml isopropanol with several NC@CNTFs immersed were sealed in the autoclave, and kept at 200 °C for 10 h. After that, the as-fabricated VOx@NC/CNTF was annealed under 320 °C for 2h in air to acquire vanadium pentoxide supported on NC@CNTF (VO@NC@CNTF).

Materials characterization

The morphology and microstructure of samples were characterized by Field emission scanning electron microscopy (FE-SEM, Phenom XL) and high-resolution transmission electron microscopy (HRTEM, Talos F200X G2) equipped with energy dispersive spectroscopy (EDS) for elemental analysis. X-ray photoelectron spectroscopy (XPS) was collected through PerkinElmer PHI 1600 ESCA. The binding energy scale was calibrated from the hydrocarbon contamination using the C1s

peak at 284.8 eV. Raman spectrum was performed on LabRAM HR Evolution microscope (Horiba Jobin Yvon) with a 532 nm laser. EPR spectra were recorded at room temperature with a Bruker EMXplus-6 spectrometer. Ex-situ SAXS (Small angle X-ray scattering) data were collected on Xeuss 3.0 using 2D image plate detector. The 2D data were integrated to simulate a 1D pattern using the Fit2D software. Ex-situ SXAS measurements were performed using X-rays of wavelength λ = 1.341 Å with a Perkin-Elmer 2D plate detector in 1 min interval. the 2D diffraction patterns were radially integrated and converted to intensity versus 2θ format using the GSAS-II software. For convenience, the 2θ values shown in this paper were converted to those corresponding to common laboratory Cu Kα radiation (λ = 1.542 Å).

Electrochemical Measurements

The multifunctional electrochemical workstation of CHI 760E was used to provide the cyclic voltammetry (CV) curves and electrochemical impedance spectra (EIS) in the frequency range of 100–0.01 kHz. Electrochemical performance, including rate capability and long-term cyclability, was measured by a battery measurement device (LAND CT2001A) at room temperature. For symmetric batteries, two pieces of pure Zn wire or Zn@CNTF electrodes were directly employed as the electrodes.

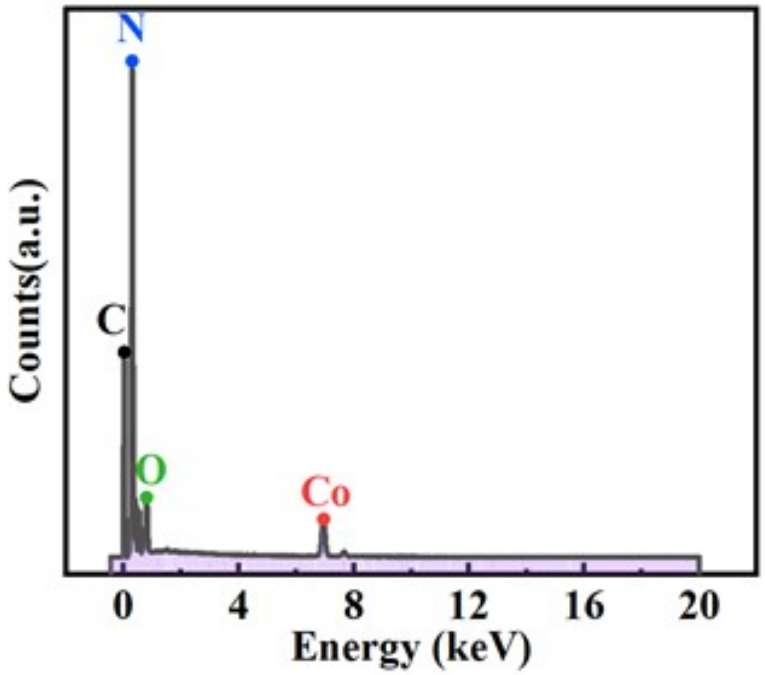

Figure S1. SEM energy dispersive profile of Co-MOF@CNTF.

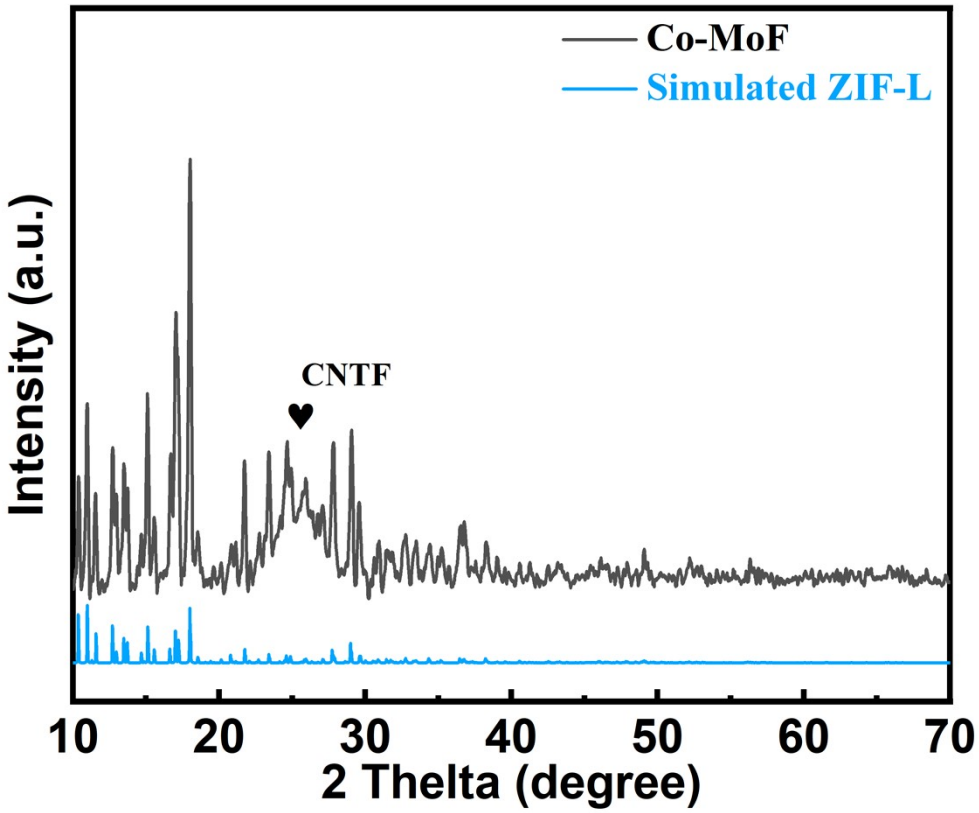

Figure S2. The XRD pattern of Co-MOF@CNTF.

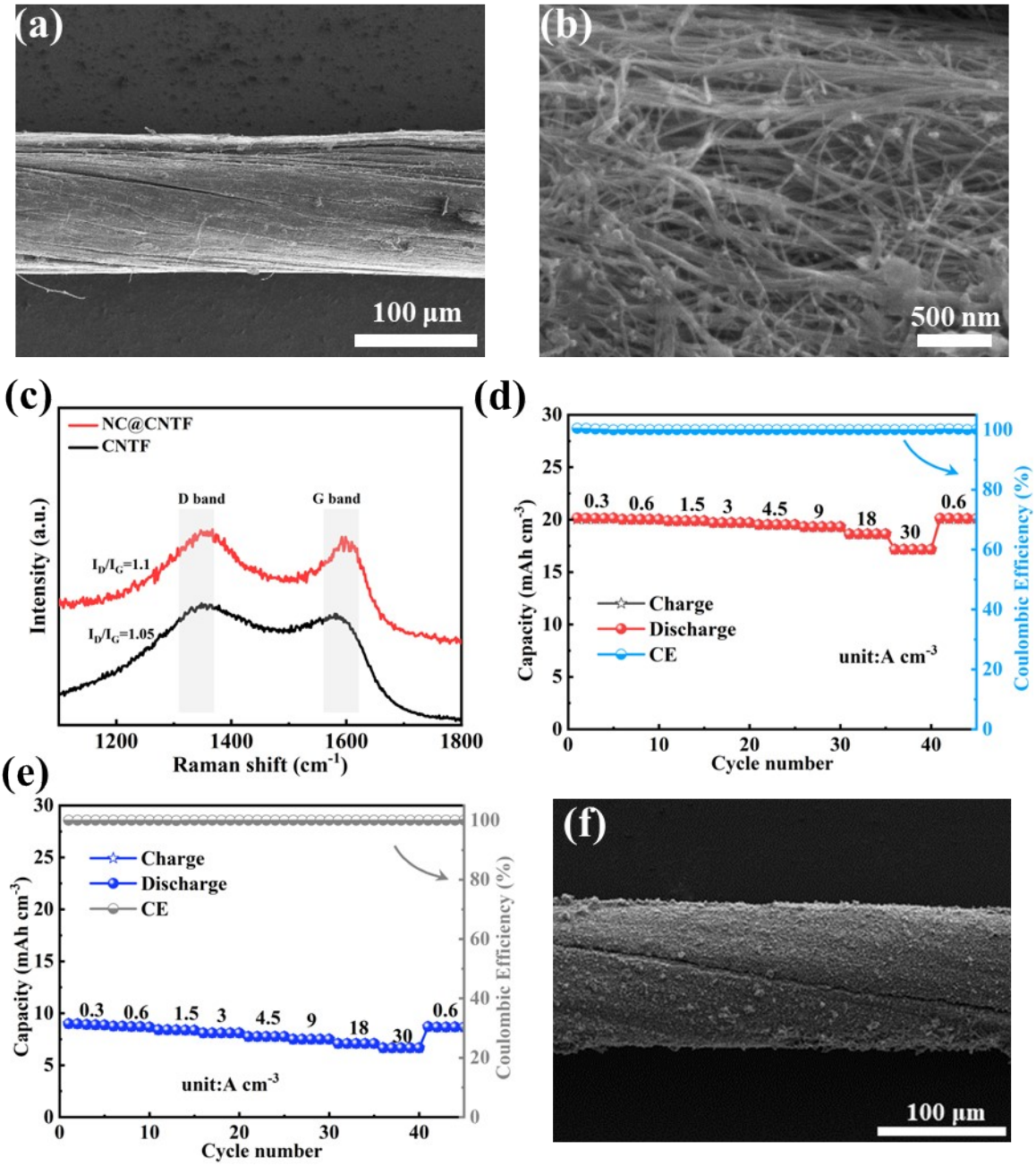

Figure S3. The low-magnification (a) and high-magnification (b) SEM image of CNTF. (c) The Raman spectra comparison of CNTF and NC@CNTF. (d) The rate performance of NC@CNTF. (e) The rate performance of CNTF. (f)The low-magnification SEM image of VN@NC@CNTF.

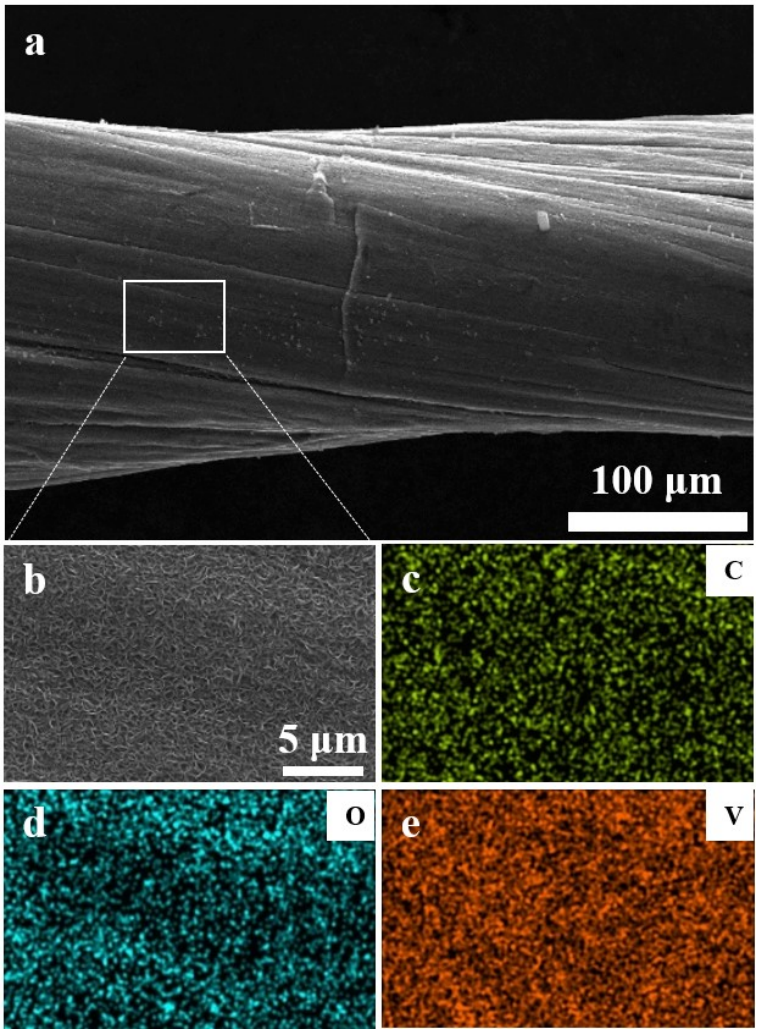

Figure S4. The SEM morphological characterization and corresponding elemental mapping of VO@CNTF.

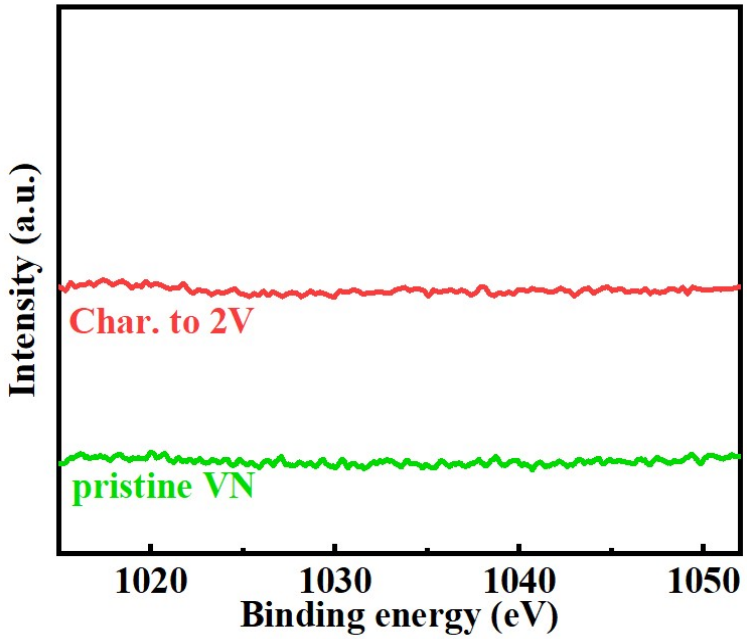

Figure S5. Zn 2p fine XPS spectra of VN@NC@CNTF and VN@NC@CNTF charged to 2V.

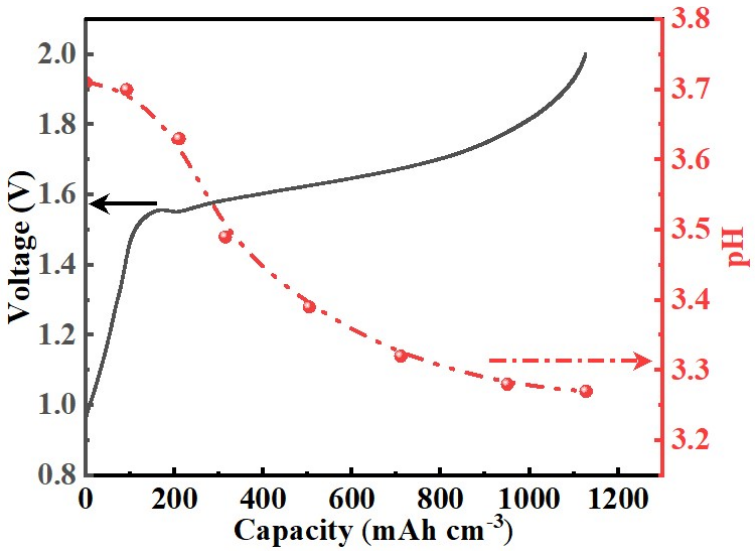

Figure S6. pH evolution of the electrolyte chemical conversion chemistry of VN@NC@CNTF at various oxidized states.

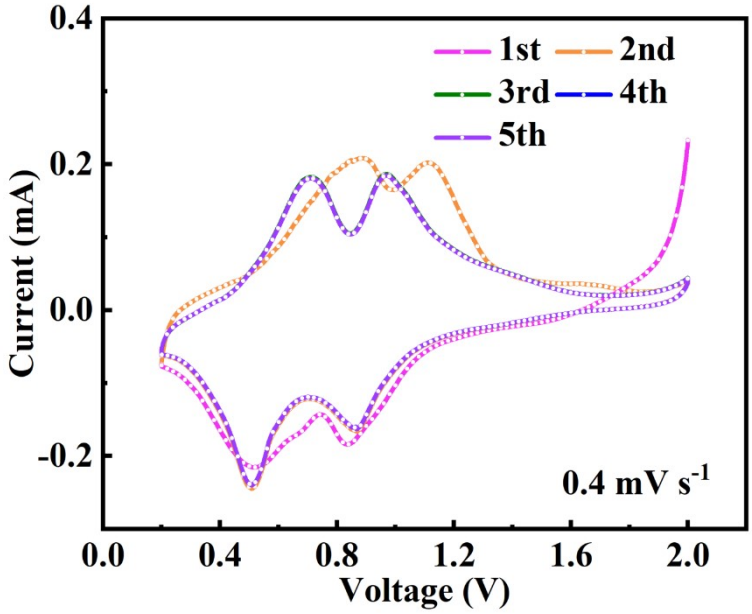

Figure S7. First five cycles of CV curves of DVOH@NC@CNTF after electrochemical oxidation.

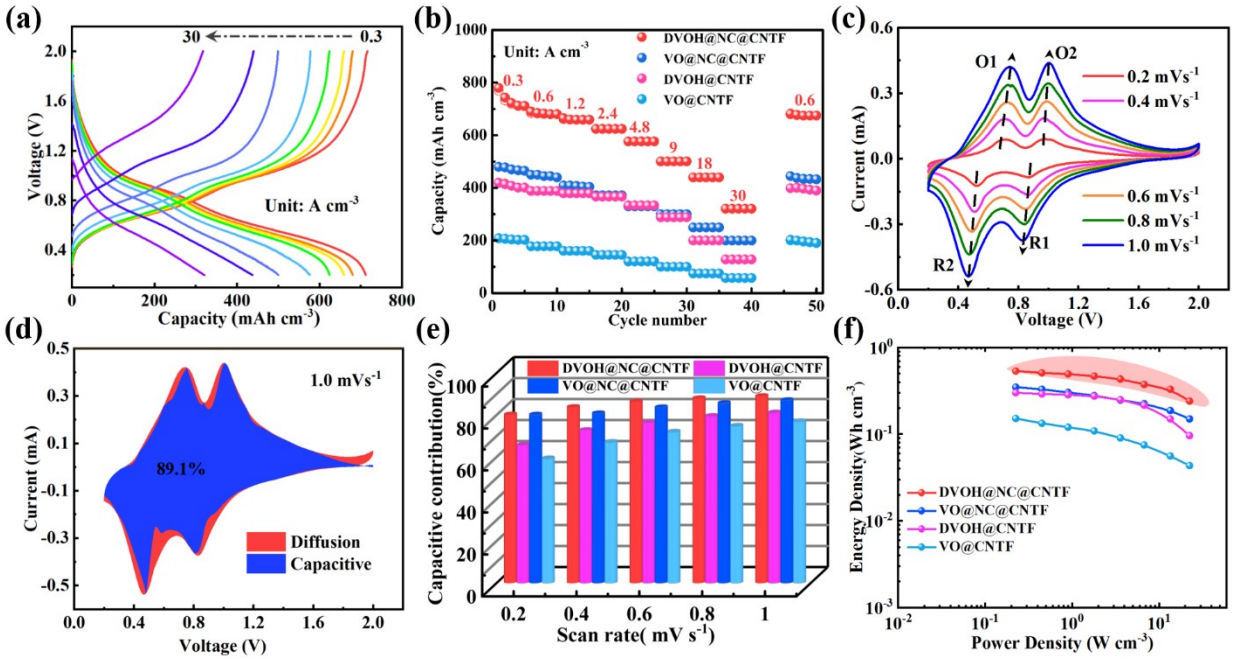

Figure S8. (a) GCD curves at various current densities of DVOH@NC@CNTF cathodes. (b) Galvanostatic rate comparison of DVOH@NC@CNTF, VO@NC@CNTF, DVOH@CNTF, and VO@CNTF four cathodes. (c) CV of DVOH@NC@CNTF cathodes at different scan rates. (d) Capacitive contribution ratio of DVOH@NC@CNTF, VO@NC@CNTF, DVOH@CNTF, and VO@CNTF four cathodes. (e) Capacitive and diffusion contribution to charge storage of DVOH@NC@CNTF at 1 mV s^{-1}. (f) Ragone plot of DVOH@NC@CNTF, VO@NC@CNTF, DVOH@CNTF, and VO@CNTF cathodes.

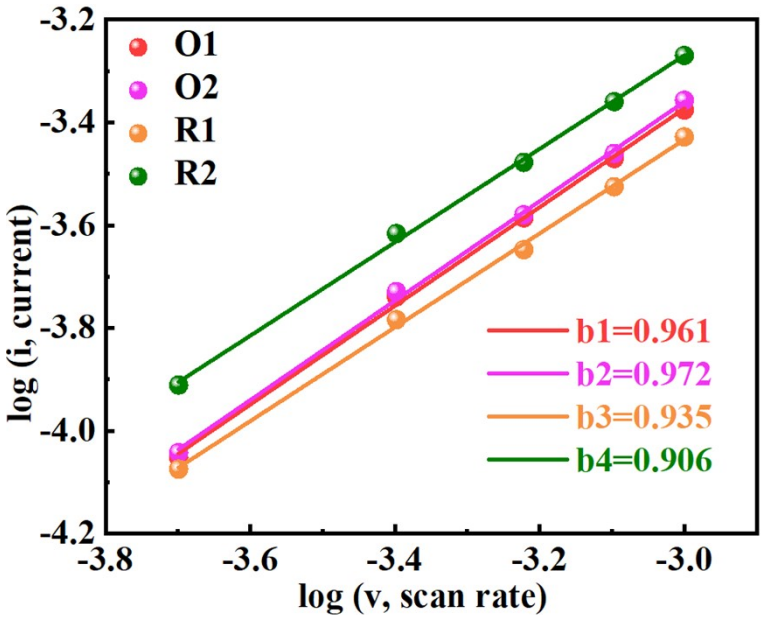

Figure S9. The calculated b-values from CV curves at different scan rates of DVOH@NC@CNTFs.

The total stored charge from capacitive processes could also be quantified by *b*-value calculated from the power law, i.e., $i = av^b$ (where a and b are changeable parameters, i stands for peak current and v represents the sweeping rate). Specifically, the *b*-values of peak currents can be determined by the slope of the log(v)–log(i) plots, which distinguishes the types of the charge storage mechanism: a b-value of 1.0 represents a typical capacitive process, whereas 0.5 indicates a total diffusion-controlled process. **Figure S9** shows that the two anodic peaks (O1 and O2) and cathodic peaks (R1 and R2) exhibit b values of 0.961, 0.972, 0.935 and 0.906 respectively, which tells an excellent extent of the capacitive behavior.

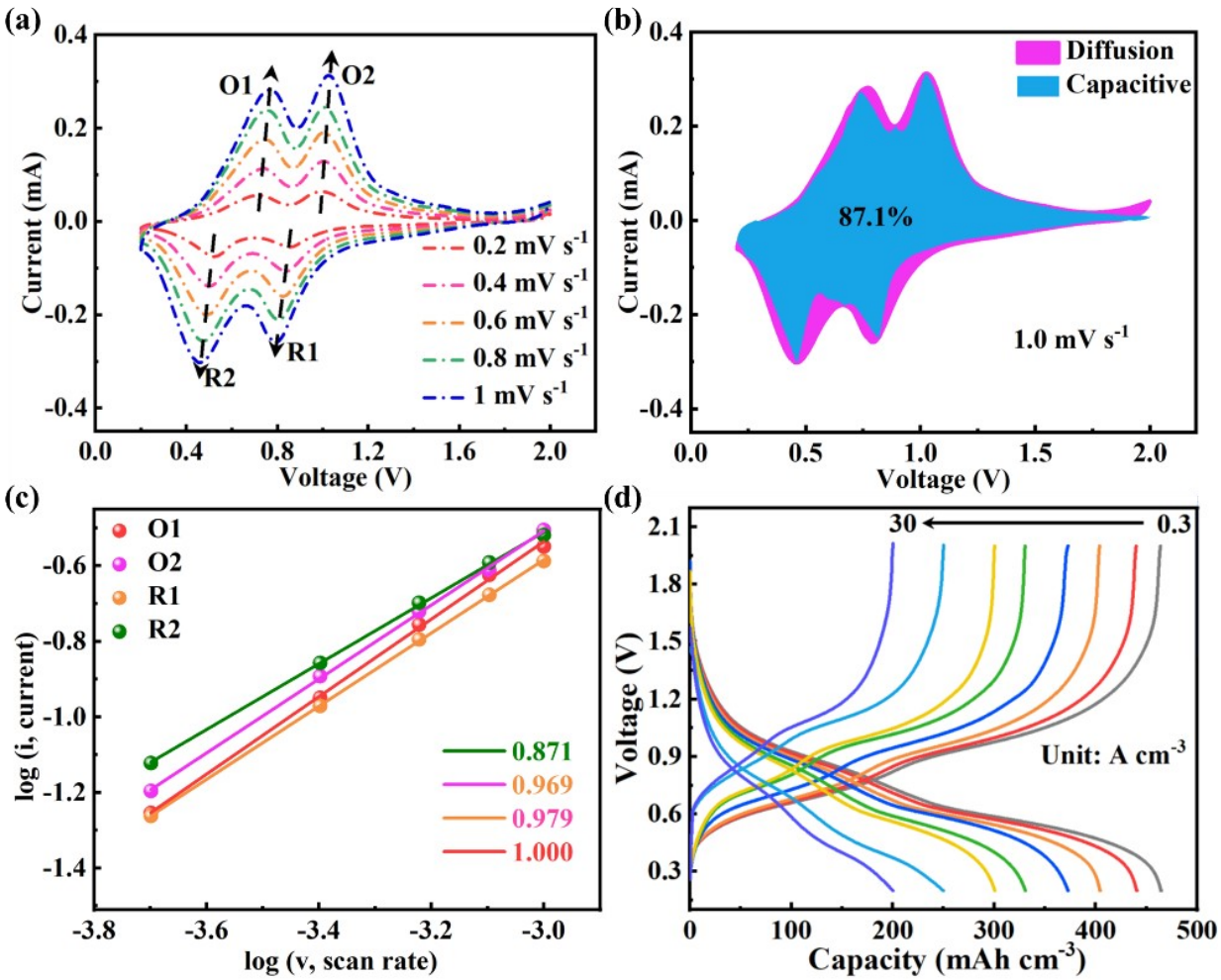

Figure S10. (a) CV of VO@NC@CNTF cathode at different sweeping rates. (b) Capacitive (blue-shaded area) and diffusion (red-shaded area) contribution to charge storage of VO@NC@CNTF at 1 mV s^{-1}. (c) The calculated b-values from CV curves at different scan rates of VO@NC@CNTFs. (d) GCD curves at various current densities of VO@NC@CNTF.

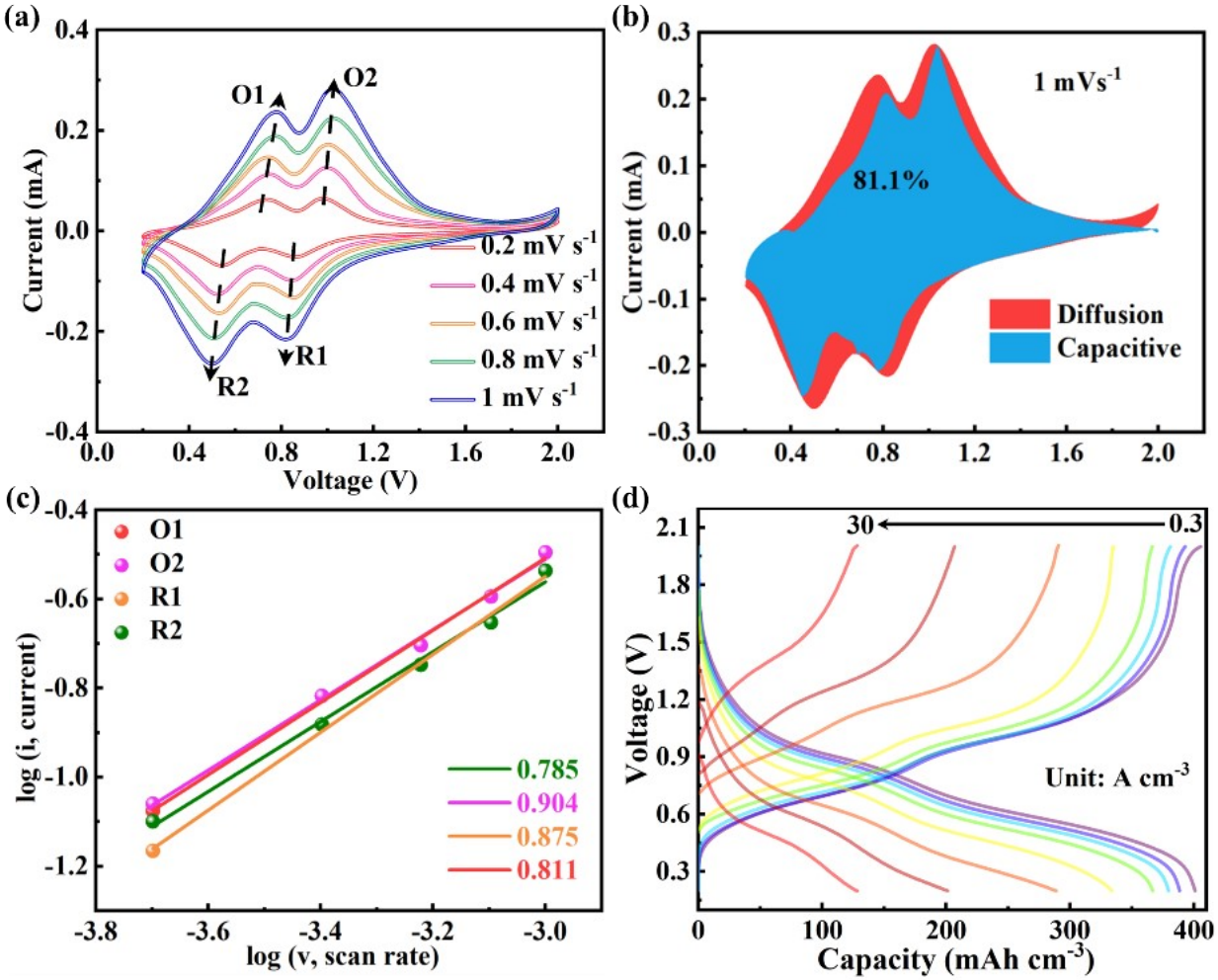

Figure S11. (a) CV of DVOH@CNTF cathode at different sweeping rates. (b) Capacitive (blue-shaded area) and diffusion (red-shaded area) contribution to charge storage of DVOH@CNTF at 1 mV s^{-1}. (c) The calculated b-values from CV curves at different scan rates of DVOH@CNTFs. (d) GCD curves at various current densities of DVOH@CNTF.

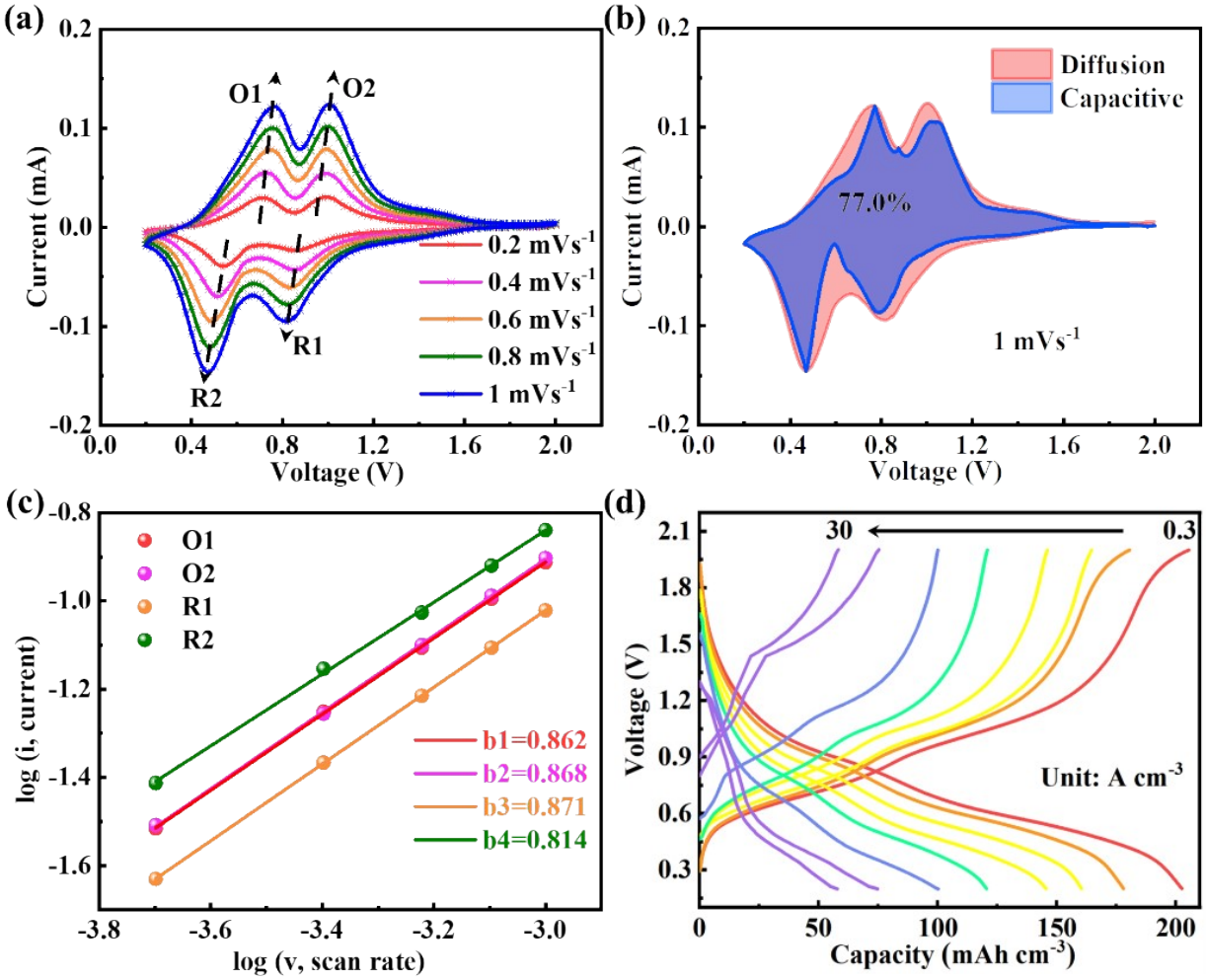

Figure S12. (a) CV of VO@CNTF cathode at different sweeping rates. (b) Capacitive (blue-shaded area) and diffusion (red-shaded area) contribution to charge storage of VO@CNTF at 1 mV s^{-1}. (c) The calculated b-values from CV curves at different scan rates of VO@CNTFs. (d) GCD curves at various current densities of VO@CNTF.

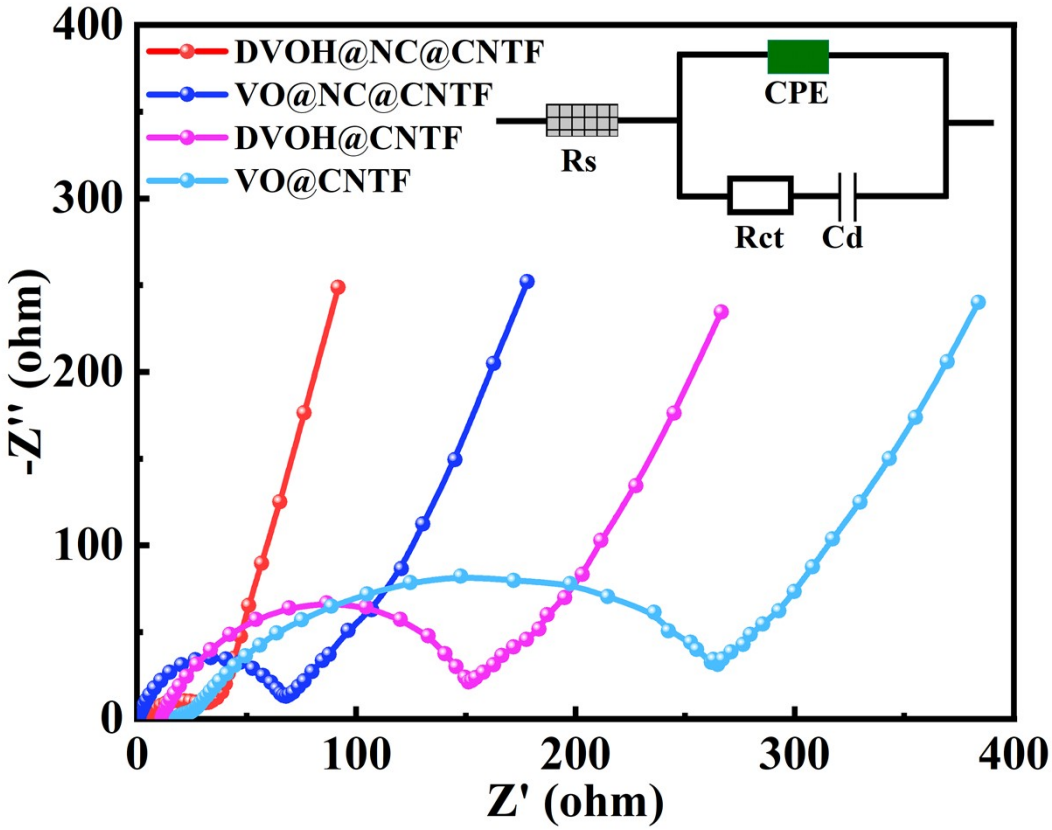

Figure S13. EIS spectra comparisons of DVOH@NC@CNTF, VO@NC@CNTF, DVOH@CNTF and VO@CNTF.

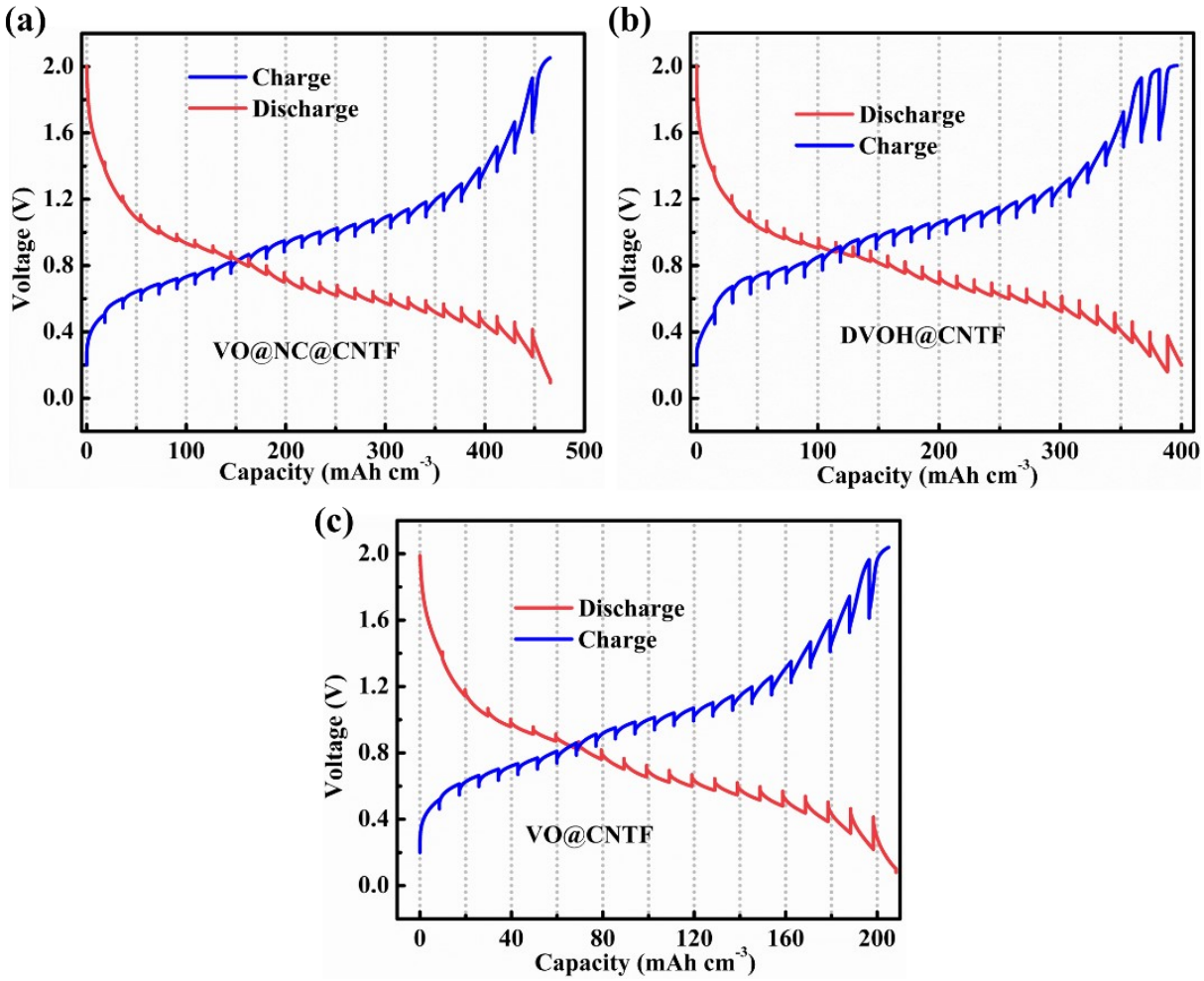

Figure S14. GITT curves of (a)VO@NC@CNTF. (b) DVOH@CNTF. (c) VO@CNTF.

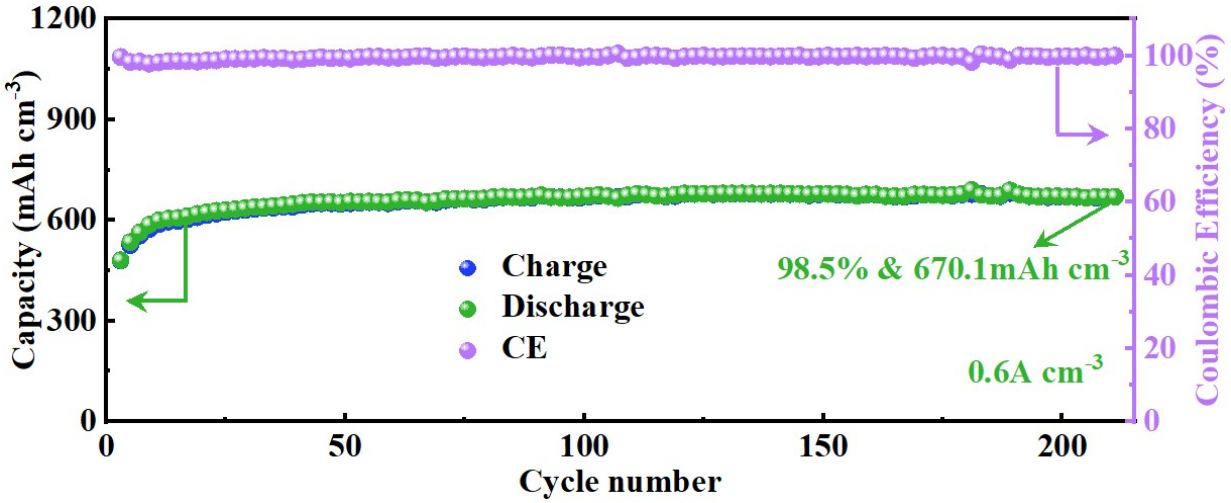

Figure S15. Cycling performance of DVOH@NC@CNTF electrode at 0.6Acm^{-3}.

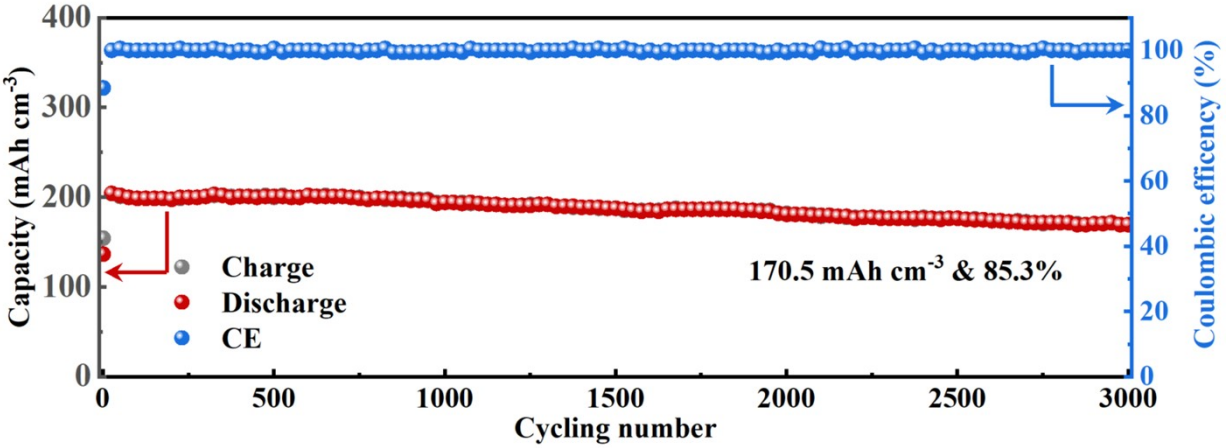

Figure S16. Cycle lifetime of VO@NC@CNTF electrode at 30 Acm^{-3}.

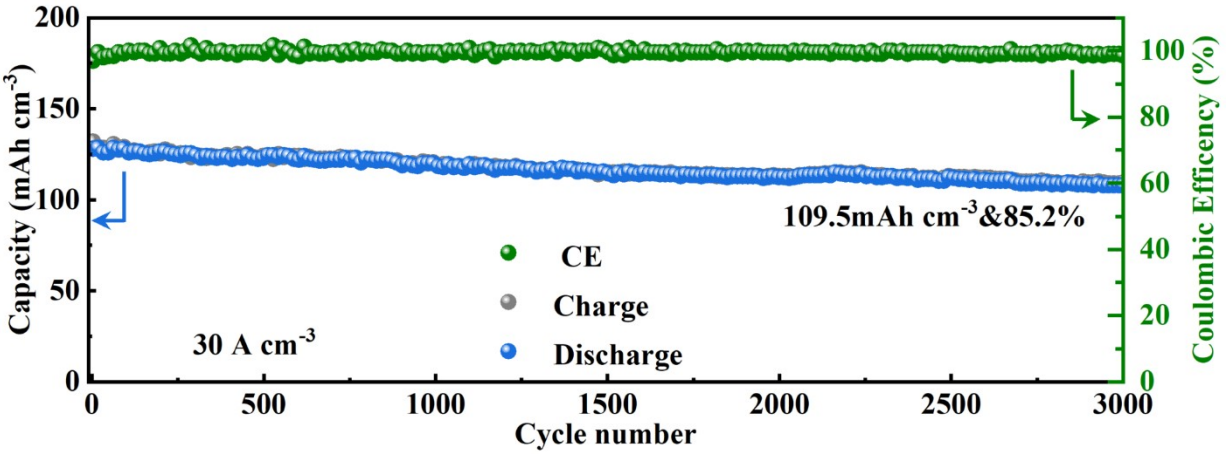

Figure S17. Cycle lifetime of DVOH@CNTF electrode at 30Acm^{-3}.

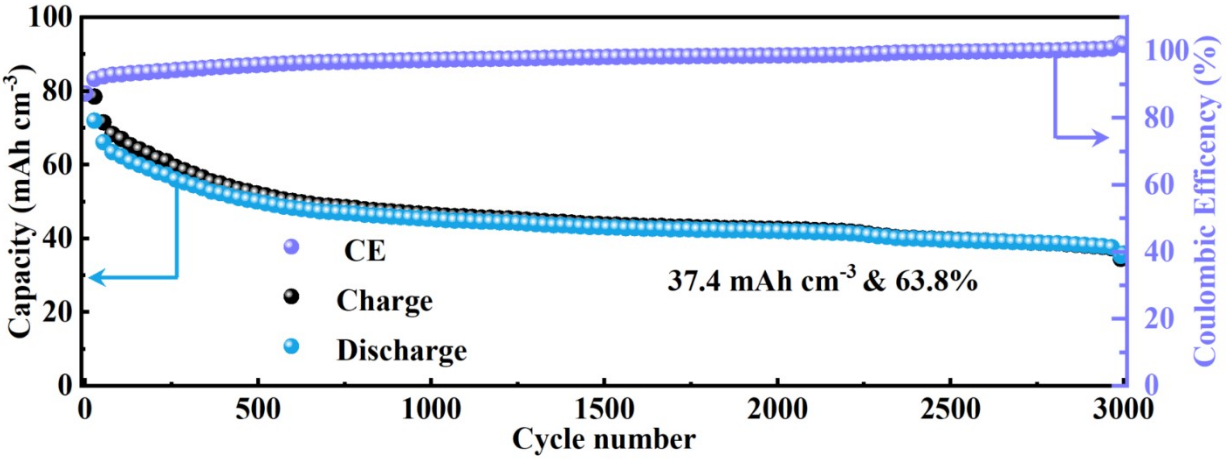

Figure S18. Cycle lifetime of VO@CNTF electrode at 30Acm^{-3}.

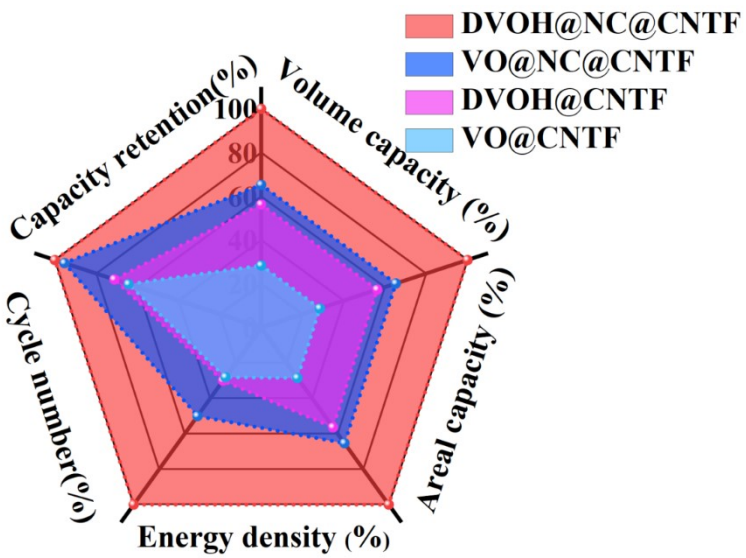

Figure S19. The stereogram of electrochemical performance for four cathodes with respect to DVOH@NC@CNTF, VO@NC@CNTF, DVOH@CNTF, and VO@CNTF.

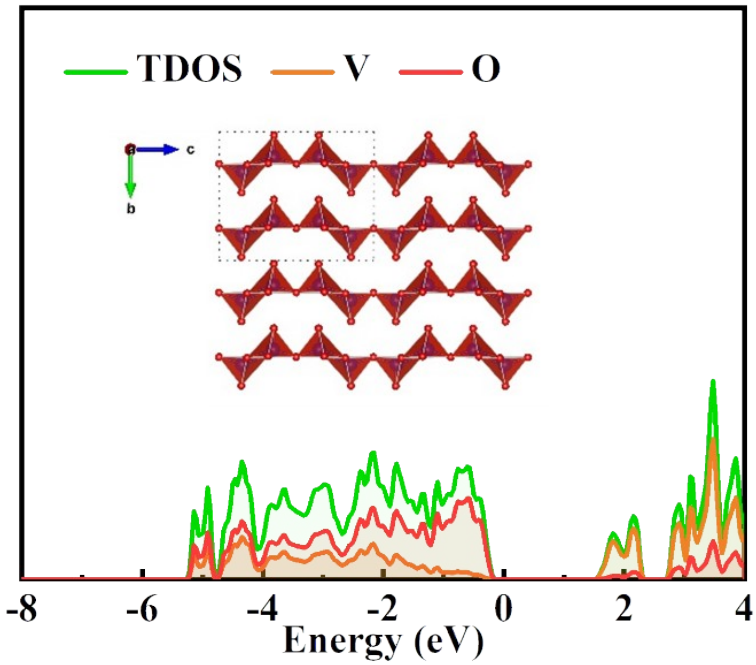

Figure S20. Calculated DOS of the orthorhombic VO (Inset is the crystal structure of V_2O_5).

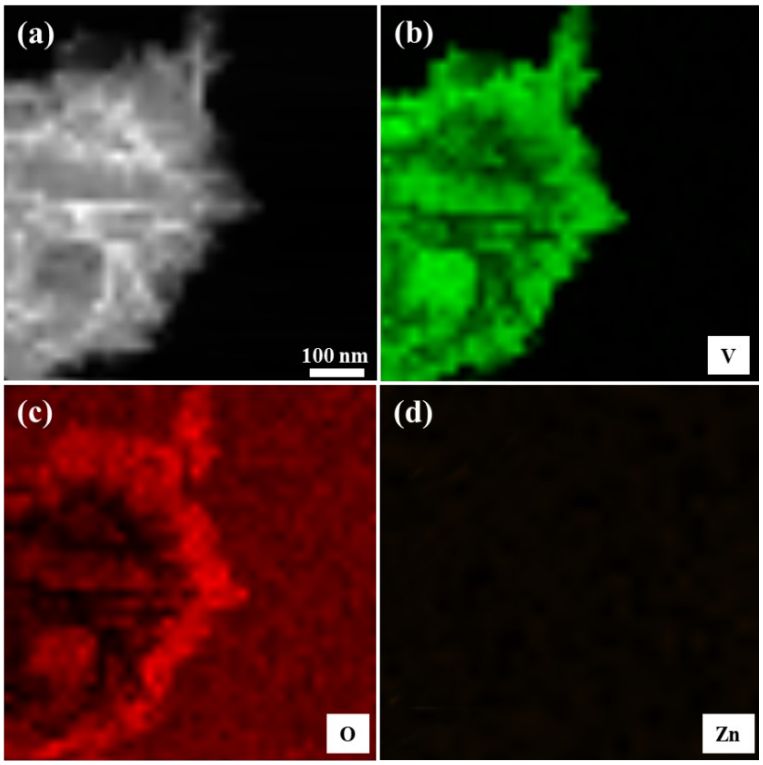

Figure S21. (a) TEM image of DVOH nanosheets and the corresponding elemental mappings of (b) V, (c) O, and (d) Zn at fully charged state.

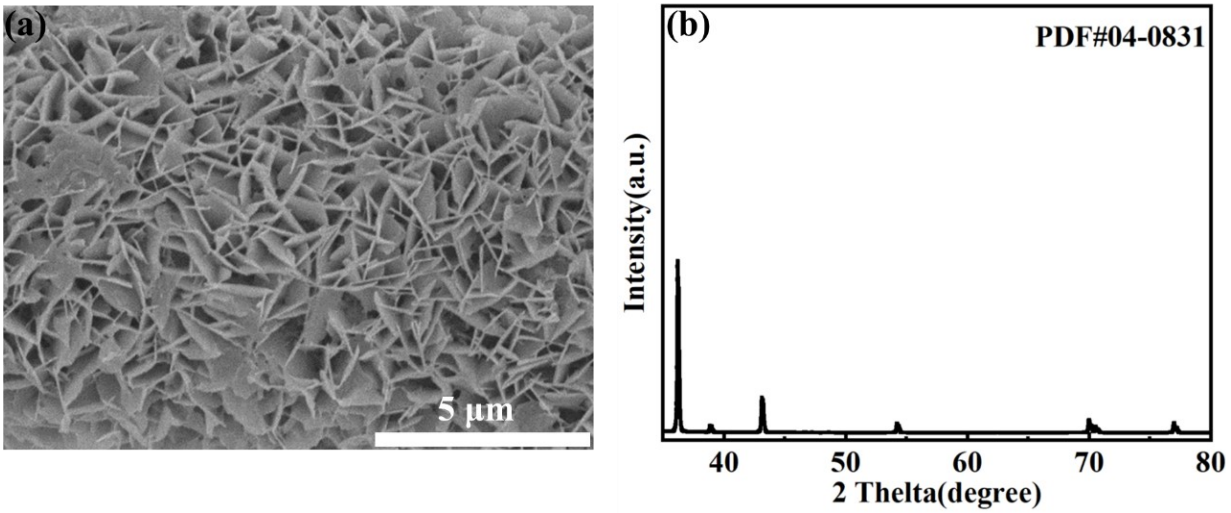

Figure S22. (a) The SEM and (b) XRD patterns of Zn@CNTF.

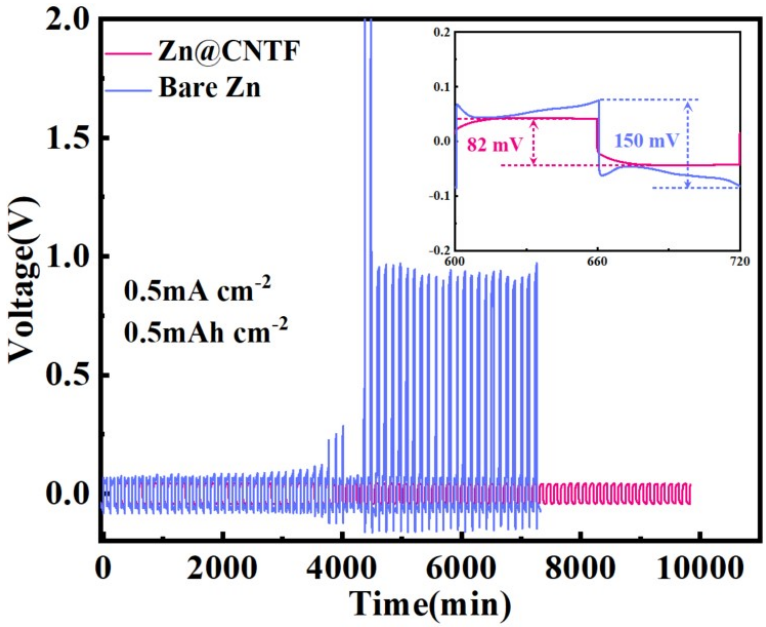

Figure S23. Cycling stability of bare Zn||Zn symmetric cells and Zn@CNTF||Zn@CNTF symmetric cells at 0.5 mA cm^{-2} with a capacity of 0.5 mAh cm^{-2}. Inset, the detailed voltage profiles of cells with bare Zn (purple) and Zn@CNTFs (red) electrodes.

Figure S23 exhibited the galvanostatic cycling performance of Zn|Zn$(CF_3SO_3)_2$|Zn symmetric cells with bare (purple lines) and CNTFs supported (red lines) Zn electrodes at a current density of 0.5 mA cm^{-2}. The Zn@CNTFs cell demonstrated relatively lower polarization than the bare Zn one (82 vs 150 mV, inset of **Figure S23**), deriving possibly from its high-conductivity of CNTFs. Moreover, the remarkably improved cycling stability of the Zn@CNTFs cells were also observed, for a low energy barrier for metal nucleation was achieved by flexible CNTFs supporters and benefited a much uniform metal plating process.

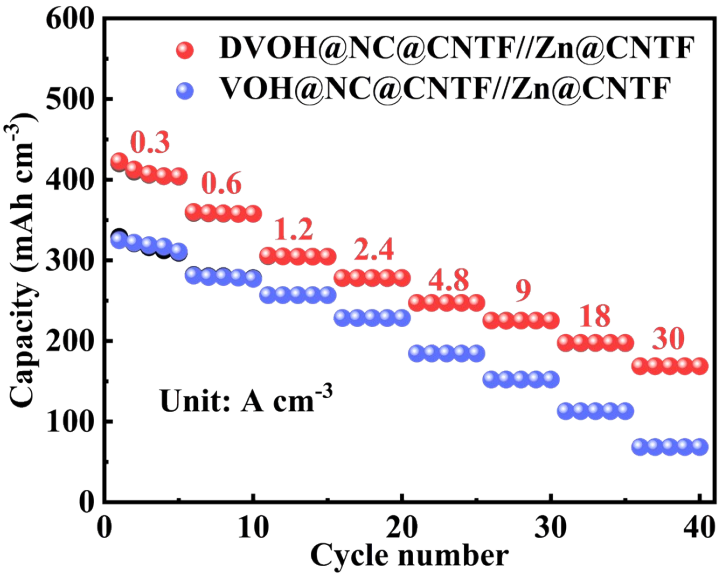

Figure S24. Galvanostatic rate comparison of DVOH@NC@CNTF and VOH@NC@CNTF FAZIBs.

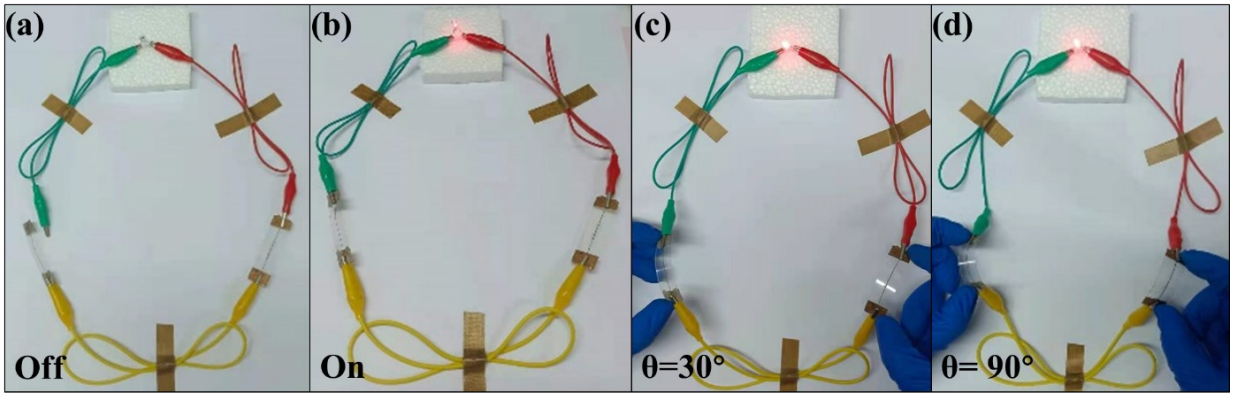

Figure S25. Flexibility test photographs of two series-connected DVOH@NC@CNTF||Zn@CNTF FAZIBs to light a red LED.

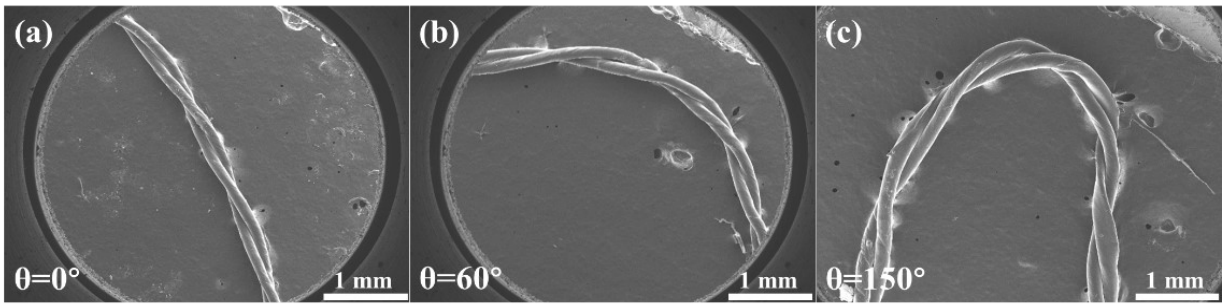

Figure S26. The SEM morphology of twisted-structure FAZIBs at different bending angles.